Microphysical characteristics of precipitation within convective overshooting over East China observed by GPM DPR and ERA5

Nan Sun[1], Gaopeng Lu[1], Yunfei Fu[1]

[1]School of Earth and Space Sciences, University of Science and Technology of China, Hefei, 230026, China

Corresponding to: Yunfei Fu, fyf@ustc.edu.cn

Abstract. We examine the geographical distribution and microphysical three-dimensional structure of convective overshooting over East China by matching Global Precipitation Measurement Dual-frequency Precipitation Radar instrument (GPM DPR) with European Centre for Medium-Range Weather Forecasts 5th Reanalysis (ERA5). Convective overshooting mainly occur over Northeast China (NC) and northern Middle and East China (MEC) and its frequency varies from 4×10^{-4} to 5.4×10^{-3}. Radar reflectivity of convective overshooting over NC accounts for a higher proportion below the freezing level, while MEC and South China (SC) account for a higher proportion above the freezing level, indicating stronger upward motion and more ice crystal particles. The microphysical processes within convective overshooting are unique, leading to various properties of the droplets in precipitation. Droplets of convective overshooting are large, but sparse, with an effective droplet radius of nearly 2.5 mm below 10 km, which is about twice that of non-overshooting precipitation. Findings of this study may have important implications for the microphysical evolution associated with convective overshooting, and provide more accurate precipitation microphysical parameters as input for model simulations.

1 Introduction

Convective overshooting provides a rapid transport mechanism that can irreversibly transport water vapor and chemical constituents from lower troposphere to the upper troposphere and lower stratosphere (UTLS) by mixing them with environmental air (Fueglistaler et al., 2004; Frey et al., 2015), which has a direct impact on radiation balance and global climate change (Solomon et al., 2010). As one of the main sources of ozone destroying OH hydroxyl radicals, stratospheric water vapor can help to destroy ozone, which has potential effects on radiative forcing (Anderson et al., 2012). Water vapor enters the stratosphere mainly through the tropical tropopause layer. Several studies show that tropical convective overshooting has a net dehydrating effect on the stratospheric humidity (Danielsen, 1993; Sherwood and Dessler, 2001), while modeling and observational studies have universally show tropical convective overshooting hydrating the stratosphere (Chaboureau et al. 2007; Jensen et al. 2007; de Reus et al. 2009; Avery et al. 2017) because of the injection of ice mass into the stratosphere (Grosvenor et al., 2007; Corti et al., 2008; Chemel et al., 2009; Khaykin et al., 2009). In midlatitude, observations and model simulations show that deep convective overshooting is also an important source for the lower stratospheric water vapor (Liu and Liu, 2016; Smith et al., 2017; Liu et al., 2020; Werner et al., 2020; Wang et al., 2023). Wang et al. (2023) use a high-resolution numerical model to study convective overshooting moistening in the midlatitude lower stratosphere and results show that convective water vapor plumes above 380-K temperature are stable in the stratosphere, while that closer to the tropopause and cloud tops are less stable. In addition to these impacts on water vapor, the effects of convective overshooting on the temperature of the UTLS have also attracted much attention (Sherwood et al., 2003; Chae et al., 2011; Biondi et al., 2012). Given these potentially significant impacts, it is of high importance to understand the characteristics of convective overshooting, which have attracted considerable attention in recent years (Johnston et al., 2018; Muhsin et al., 2018).

Perhaps one of the most poorly understood features of convective overshooting is the microphysical structure of precipitation, such as particle size, concentration, phase state and other parameters. Understanding the microphysical characteristics of convective overshooting is helpful to clarify the efficiency of water vapor transport to the lower stratosphere by convective overshooting. And the microphysical processes within convective overshooting are closely related to storm dynamics and thermodynamics through latent heat, and the quantitative description of microphysical characteristics is

helpful to improve the accuracy of model simulation parameters (Homeyer and Kumjian, 2015). In addition, thunderstorms with overshooting tops are closely associated with hazardous weather at the Earth's surface, such as heavy rainfall, large hail, damaging winds and tornadoes (Reynolds, 1980; Negri and Adler, 1981; Fujita 1989; Kellenbenz et al., 2007; Brunner et al., 2007; Setvák et al. 2010; Dworak et al. 2012; Line et al., 2016; Bedka et al., 2018; Marion et al., 2019), indicating the application of overshooting detections for severe weather warnings (McCann 1983; Bedka, 2011; Homeyer and Kumjian, 2015). Bedka (2011) have studied relationship between overshooting cloud tops with severe weather over Europe and results show that an overshooting was found near 47% of the confirmed severe weather events. Specifically, overshooting top-severe weather relationship is strong for large hail (53%) and severe wind (52%) but relatively weak for tornado events (14%). Dworak et al. (2012) show that severe weather was often associated with overshooting detections during warm season (April-September). Furthermore, convective overshooting generates gravity waves, and gravity wave breaking generates turbulence, which is of fundamental importance in the generation of small-scale motions that influence aircraft (Lane and Sharman, 2006). Tens of commercial airline passengers are injured each year over the continental United States during turbulence-related aviation incidents (Lane et al., 2003). Cloud-to-ground lightning is also found to occur frequently near convective overshooting region, which is also a threat to aviation safety (Bedka, 2011). In summary, hazardous weather accompanied by convective overshooting have serious harm to social economy and human production and life. Quantitative study of the precipitation structure of convective overshooting can help figure the relationship between convective overshooting and severe weather like heavy rainfall out, providing a predictor for severe weather warning and ensuring aviation safety. Liu et al. (2012) studied the climatological characteristics of convective overshooting and found convective overshooting show remarkable regionality and seasonal variations. Homeyer and Kumjian (2015) observed the radar reflectivity characteristics of convective overshooting from the analysis of the polarimetric radar observations. Although the above studies have explored the characteristics of some precipitation parameters within convective overshooting, we still lack the understanding of more precipitation microphysical parameters and more detailed microphysical processes within convective overshooting due to the limitations of observation methods.

To fully study the microphysical characteristics of convective overshooting, accurate methods of detecting the frequency and long-term distribution of convective overshooting are required. The

82 traditional way for detecting convective overshooting from satellite is to find pixels in infrared imagery

83 with brightness temperatures colder than a given temperature threshold (Machado et al. 1998; Rossow

84 and Pearl 2007). Gettelman et al. (2002) have studied the cloud regions colder than the tropopause

85 temperature on infrared images and found that the frequency of tropical convective overshooting is about

86 0.5%. However, it is impossible to guarantee that the low value of infrared brightness temperature

87 represents clouds penetrating the tropopause rather than cirrus or cloud anvil in the upper air due to the

88 lack of vertical structure information of convection. Also, overshoots mix with relatively warm

89 stratosphere air such that cold pixels are often diminish and not a reliable means to identify overshooting.

90 With the launch of Precipitation Radar aboard Tropical Rainfall Measuring Mission (TRMM),

91 three-dimensional structure information of precipitation within the convective overshooting can be

92 provided (Alcala and Dessler, 2002; Liu and Zipser, 2005) and a new method for detecting the

93 convective overshooting is proposed that is to find pixels with rain top height higher than tropopause

94 height (Xian and Fu, 2015; Sun et al., 2021), which improves the accuracy of detecting convective

95 overshooting. Still, TRMM PR can't provide the precipitation microphysical information, which limits

96 our study on the internal microphysical structure within convective overshooting. Besides, TRMM PR

97 can underestimate the height of convective overshooting because of only sensitive to large precipitation

98 particles (sensitivity at ~17 dBZ) (Hanii and Zheng, 2014).

99 As the continuation of TRMM PR, Global Precipitation Measurement (GPM) carrying the first

100 Dual-frequency Precipitation Radar (DPR) launched in February 2014. GPM DPR include two bands of

101 precipitation radar, which provides excellent opportunities for studying the microphysical structure of

102 precipitation (Sun et al., 2022a). Liu et al. (2016, 2020) have used GPM KuPR and ERA-Interim

103 6-hourly dataset to study climatology and detection of convective overshooting. However, the above

104 studies only use the KuPR data and mainly focus on the geographical distribution; the vertical and

105 microphysical precipitation structure of convective overshooting remains unknown.

106 East China is a densely populated area, an economic concentration area and an important food

107 producing area in China. Affected by the circulation anomalies of the East Asian tropical and subtropical

108 monsoon and their interactions, extreme precipitation events occur frequently over East China. Many

109 scholars have studied the characteristics of precipitation in East China (Zhang et al., 2018; Xu, 2020), but

110 few have studied the characteristics of convective overshooting and its internal precipitation

111 microphysical structure over East China, which can not only help the flood prevention work in summer

112 over East China, but also ensure social economic development to a certain extent. In addition, there are

113 thousands of airlines over East China, carrying hundreds of millions of passengers every year. In view

114 of the impact of convective overshooting on social economic and aviation safety, it's necessary to

115 conduct relevant research on East China. The purpose of this study is to examine the microphysical

116 characteristics of convective overshooting over East China by matching the precipitation data from GPM

117 DPR and meteorological parameters from ERA5. We will focus on the vertical structure of precipitation

118 within convective overshooting and further explore its microphysical structure feature of precipitation.

119 **2 Data and method**

120 **2.1 DPR-based precipitation dataset**

121 GPM DPR include KuPR (Ku band, 13.6 GHz) and KaPR (Ka band, 35.5 GHz), two bands of

122 precipitation radar. KuPR is similar to TRMM PR and has a longer wavelength, which is better at

123 detecting heavy precipitation (the minimum detected precipitation is about 0.5 mm/h). However, KaPR

124 has a shorter wavelength, which is more sensitive to weak precipitation (the minimum detected

125 precipitation is about 0.2 mm/h). Based on the different echo characteristics of Ku band and Ka band, the

126 dual channel inversion algorithm can be used to retrieve Droplet Size Distribution (DSD). Here we use

127 the precipitation datasets are provided by the GPM level 2 product 2ADPR in version 6. The horizontal

128 resolution is 5 km and the vertical resolution is 125m. The precipitation microphysical parameters

129 provided by GPM 2ADPR include droplet concentration (dBN_0) and effective radius (D_0).

130 **2.2 ERA5-based meteorological dataset**

131 The meteorological data are from ERA5 reanalysis product, whose name is "ERA5 hourly data on

132 pressure levels from 1940 to present". And the following parameters are used in this paper: temperature,

133 specific humidity, vertical velocity, U-component of wind, and V-component of wind. The time

134 resolution is 1 h and the horizontal resolution is $0.25\,° \times 0.25\,°$. Vertical coverage is 1000 hPa to 1hPa

135 and vertical resolution is 37 pressure levels (1000, 975, 950, 925, 900, 875, 850, 825, 800, 775, 750,

136 700, 650, 600, 550, 500, 450, 400, 350, 300, 250, 225, 200, 175, 150, 125, 100, 70, 50, 30, 20, 10, 7, 5,

137 3, 2, 1 hPa).

2.3 Detection method of convective overshooting

138

139 Convective overshooting is defined to occur where the storm top height is above the real-time

140 tropopause height in a precipitation pixel. Obtaining correct tropopause height data with high spatial

141 and temporal resolution is the most important and difficult step in convective overshooting detection.

142 On the one hand, the determination of the tropopause is still under debate. At present, the following four

143 definitions of the tropopause are widely adopted throughout the world: Cold point tropopause, thermal

144 tropopause, dynamic tropopause and ozone tropopause. Cold point tropopause is only physically

145 meaningful in the latitude zone $10°S-10°N$ near the equator (Highwood and Hoskins, 1998;

146 Rodriguez-Franco and Cuevas, 2013). Dynamic tropopause is based on the differing values of potential

147 vorticity in the troposphere and stratosphere, which applies to extratropical areas (Danielsen et al.,

148 1987; Holton et al., 1995). Ozone tropopause is defined based on the ozone sounding profiles, whose

149 disadvantage is that the choice of ozone mixing ratio thresholds varies with region and season (Bethan

150 et al., 1996; Zahn et al., 2004). Therefore, this paper uses the thermal tropopause, which is defined by

151 the World Meteorological Organization (WMO) (WMO, 1957). The thermal tropopause is based on the

152 temperature lapse rate, also known as lapse-rate tropopause. The accurate calculation of the tropopause

153 height based on this definition, on the other hand, depends on the temperature profile data with high

154 spatial and temporal resolution. The latest generation of reanalysis data ERA5 provides hourly estimates

155 of a large number of atmospheric, land and oceanic climate variables, which has attracted much attention

156 due to its much higher spatial and temporal resolution than its predecessor ERA-Interim, especially in the

157 upper troposphere and lower stratosphere (Hoffmann et al. 2019). Sun et al. (2022b) verified the

158 accuracy for the tropopause height calculated from temperature profiles of ERA5 by comparing ERA5

159 with other popular datasets. Based on the above analysis, the process of convective overshooting

160 detection is shown as follows.

161 Firstly, match each pixel of GPM DPR detection with ERA5 grid data by using the principle of the

162 nearest method. The marching time between GPM and ERA5 is 1 h, and the matching range is $0.25° \times$

163 $0.25°$. Storm top height is obtained from the GPM DPR.

164 Secondly, real-time tropopause height is calculated from the temperature profiles from ERA5

165 according to the definition from the World Meteorological Organization (WMO, 1957). The

166 algorithmic process is shown as follows: Firstly, find X layer whose atmospheric lapse rate is 2 K km^{-1}

167 or less starting from the first layer (near the ground) of the temperature profile, and then judge whether

168 the atmospheric lapse rate does not exceed 2 K km^{-1} between the X level and all higher levels within 2

169 km, if so, the height of X layer is the tropopause height, if not, repeat the above algorithm starting from

170 the X layer until tropopause layer is found.

171 At last, convective overshooting is identified based on the storm top height and tropopause height.

2.4 Study areas

173 The study areas are marked as black boxes in Fig. 1a and only the land parts are studied because

174 characteristics of vertical structure of precipitation over land and sea are very different, and this study

175 is limited in space and focuses only on the land region.   Using years of NCEP/NCAR reanalysis data,

176 Xia (2015) analyzed the climatic feature of temperature and water vapor in China and divided China into

177 different climatic zones. To have a better understanding of precipitation microphysical structure over

178 different regions of East China, we also divided East China into three climatic zones according to its

179 climatic characteristics and previous studies (Xia, 2015; Sun et al., 2022a). From north to south, they are

180 Northeast China (NC, 38°–50°N, 118°–130°E), Middle and East China (MEC, 26.5°–38°N, 112°–

181 123°E), and South China (SC, 18°–26.5°N, 108°–123°E). For the three regions, the lower latitude areas

182 have higher surface temperature, greater temperature lapse rate and lower temperature of stratosphere.

183 Temperature profiles of same latitude are essentially same over SC and MEC, and temperature signals

184 exist meridional differences over NC. Atmospheric humidity has remarkable regional characteristics.

185 SC is wetter, with the surface relative humidity of more than 70%, while NC and MEC are drier and

186 their humidity range from 50% to 70% (Xia, 2015). The study time frame is defined as the time from

187 2014 to 2020 in summer (June, July and August)

3 Results

3.1 Case studies

190 Three cases selected from NC, MEC and SC are analyzed to lay a foundation for the subsequent

191 statistical analysis. The precipitation characteristics of the three cases are shown as Fig. 2. The Case 1

192 (C1) occurs in NC at 14:00 on July 1, 2017. Convective overshooting is observed in a total of 65 pixels

193 for C1, whose mean rain rate are 20.7 mm/h (Fig. 2a) and mean storm top height are 14.1 km (Fig. 2b).

194 The strong radar reflectivity along A1B1 occurs at 35-95km away from point A1, and the strongest echo

195 is up to 50 dBZ, appears at 0-5 km (Fig. 2c). The maximum echo height is about 15 km, 2 km higher than

196 the tropopause height. The Case 2 (C2) occurs in MEC at 13:00 on July 30, 2015. Convective

197 overshooting is observed in a total of 58 pixels for C2,   and their mean rain rate are 29.7 mm/h (Fig. 2d)

198 and mean storm top height are 15.2 km (Fig. 2e). The radar echo along A2B2 is very strong and the

199 strongest echo is up to 50 dBZ, which is about 45-95 km away from point A2 (Fig. 2f). The highest echo

200 can reach to about 17 km altitude. The Case 3 (C3) occurs in SC at 17:00 on June 13, 2015. Convective

201 overshooting is observed in a total of 8 pixels for C3 and their mean rain rate are 46.3 mm/h (Fig. 2g) and

202 mean storm top height are 16.9 km (Fig. 2h). The strongest echo occurs at 60-70 km away from point A3

203 and the highest echo can reach to 17.2 km, about 0.5 km higher than the tropopause height (Fig. 2i).

204 To learn about the characteristics of the large scale circulation for these three cases, we calculate the

205 distribution of Precipitable Water Vapor (PWV), streamlines and Vertical Velocity (VV), and locations

206 of the three cases are shown as the black boxes in Fig. 3. In general, areas in which convective

207 overshooting occur have abundant PWV and strong ascending movement. In C1, The PWV of the region

208 in which convective overshooting occurs is between 50 and 55 mm, which is higher than otherwise (Fig.

209 3a). Upward motion near the convective overshooting is strong, ranging from -0.03 to -0.12 Pa/s,

210 contributing to the occurrence of convective overshooting (Fig. 3b). The PWV of C2 is more abundant

211 than C1, and the PWV of the area in which convective overshooting occurs are between 55 and 60 mm

212 (Fig. 3c). The VV near the convective overshooting is mostly between -0.09 and -0.15 Pa/s (Fig. 3d). In

213 C3, the PWV near the precipitation area and convective overshooting area are the most abundant

214 compared with C1 and C2, whose maximum can exceed 70 mm (Fig. 3e). Upward movement near the

215 precipitation area and convective overshooting area are very strong and the VV are between -0.12 and

216 -0.18 Pa/s, which provide abundant water vapor and dynamic conditions for the occurrence of

217 convective overshooting.

218 **3.2 Statistical results**

219 **3.2.1 Geographical distribution**

220 Firstly, the horizontal distribution characteristics of convective overshooting over East China are

221 analysed by designing a more accurate algorithm for convective overshooting determination. Accurate

222 determination of tropopause height is the first step of the convective overshooting determination

223 algorithm. We first analyze geographical distribution of climatological mean of the tropopause height

over East China calculated from ERA5, shown as Fig. 1b. In general, the tropopause height over East China is between 11.6 km and 16.7 km and has an obvious zonal distribution pattern: Tropopause height over SC and southern MEC (18-36 °N) is the highest and has small spatial variabilities, concentrated at ~16.7 km. Over northern MEC (36-38 °N), tropopause height decreases and forms a gradient, which decreases to 16 km. Tropopause height over NC is the lowest and continues to decrease in a gradient pattern from south to north, decreasing to 13 km near central NC (45 °N) and 12 km near northern NC (48 °N). Minimum standard deviation of tropopause height appears in SC, along with central and southern MEC, lower than 0.2 km. From northern MEC to northern NC, the standard deviation first increases and then decreases, reaching a maximum of more than 2 km around 42 °N, and standard deviation over NC is generally above 1 km.

Obtaining storm top height from precipitation data is the second step of convective overshooting algorithm. Fig. 4 show geographical distribution of storm top height for total precipitation, convective precipitation and convective overshooting. Total precipitation represent the all pixels with rain rate higher than 0 mm/h detected by GPM DPR, and those pixels whose rain type are "Convective" are defined as convective precipitation. As shown, mean storm top height over East China varies from 4.5 km to 8.5 km, while convective storm top height is mainly distributed between 3.5 km and 9 km. Convective storm top height over NC and northern MEC are the highest, with most areas exceeding 6.5 km and as we noted above, tropopause height in these two regions are lower (Fig. 1b), it can be inferred that convective overshooting events are more likely to occur. Further analysis of the frequency of convective overshooting in the following text will confirm this point. Compared with NC, convective storm top height over SC and southern MEC is lower, mainly distributed below 6.5 km. Storm top height of convective overshooting ranges from 10 km to 21 km (Fig. 4c), much higher than normal precipitation (total and convective precipitation) and increasing gradually from north to south. Storm top heights of convective overshooting over NC and northern MEC are low, distributed between 10 km and 16 km, which is due to a lower tropopause height (Fig. 1b) allowing convection with lower storm top height to reach the stratosphere. This lowers the mean storm top height of convective overshooting in these regions, while tropopause heights over SC and southern MEC range from 16 km to 21 km (Fig. 1b), allowing only strong convection to reach the stratosphere.

The frequency of convective overshooting is defined as the number of convective overshooting events divided by the total observed sample number of GPM DPR. Statistical results indicate that the frequency

254 of the convective overshooting over East China is very low, with a magnitude of only 10^{-3}, varying

255 regionally (Fig. 5). Sample size of convective overshooting over NC is the highest, followed by MEC,

256 and SC is the lowest (Table 1). Convective overshooting over NC and northern MEC, whose frequency

257 range from 4×10^{-4} to 5.4×10^{-3} (Fig. 5), occur more frequently than SC and southern MEC, whose

258 frequency is between 2×10^{-4} and 6×10^{-4}, which is mainly because the former has a lower tropopause

259 height and it's easier for convective overshooting to occur.

260 **3.2.2 Vertical structures**

261 Based on the reflectivity profiles and the rain-rate profiles provided by the GPM DPR instrument, we

262 studied the vertical structure of precipitation within convective overshooting. Contoured Frequency by

263 Altitude Diagrams (CFADs) analysis of radar reflectivity can effectively indicate the three-dimensional

264 structure characteristics of precipitation, which is therefore applied in a large number of precipitation

265 studies (Yuter and Houze, 1995). Fig. 6 shows CFADs of the DPR radar reflectivity. In general, radar

266 reflectivity within convective overshooting is stronger and its storm top height is higher. And the CFADs

267 analysis also shows regional differences. Radar echo intensity of convective overshooting over NC is the

268 weakest, and the echo near surface is mainly distributed from 25 dBZ to 55 dBZ, with sharp peak near 47

269 dBZ, while the peak of the total precipitation is around 16 dBZ. And the max radar echo top within

270 convective overshooting over NC can reach to 13.5 km, 3.3 km higher than the mean precipitation.

271 Compared with NC, radar reflectivity within convective overshooting over SC and MEC are stronger and

272 their CFADs character is more similar. Their echo top height is ~18 km, 6.5 km higher than total

273 precipitation, 4.5 km higher than NC, and their echo near surface concentrated around 30-55 dBZ, while

274 that of total precipitation is between 15 dBZ and 43 dBZ. Besides, Radar reflectivity of convective

275 overshooting over NC accounts for a higher proportion below the freezing level (Altitude where the

276 temperature is 0 ℃), while MEC and SC account for a higher proportion above the freezing level, which

277 indicate that the upward motion within convective overshooting over MEC and SC are stronger and there

278 are larger.

279 Quantitative analysis of the vertical structure of precipitation within convective overshooting is one of

280 the main issues of interest to this study. Shown as Fig. 7, the rain rate profiles of convective overshooting

281 are provided, and to highlight its unique feature, rain rate profiles of total precipitation and convective

282 precipitation are also given. In general, the rain rate of convective overshooting is much higher,

283 especially below the freezing level (~5 km), 5-10 times that of normal precipitation. This indicates

284 stronger convection and a greater concentration of ice. In addition, differences between three regions are

285 obvious. Rain rate of convective overshooting over NC are about half as high as over MEC and SC,

286 which is consistent with the results of radar echo. At 1 km altitude, rain rate of convective overshooting

287 are 12 mm/h (NC), 22.5 mm/h (MEC), and 23 mm/h (SC) respectively. Below freezing level, the

288 variation of rain rate with altitude is not very obvious, and difference of rain rate between convective

289 overshooting and normal precipitation are ~8 mm over NC and ~20 mm over MEC and SC. Above

290 freezing level, rain rate of convective overshooting clearly decreases with increasing altitude, and rain

291 rates are 6mm/h (NC), 10 mm (MEC) and 6.5mm (SC) at 10 km. However, rain rates of other

292 precipitation are no more than 2 mm/h above 8 km, we therefore suggest that the strong upward flow

293 within convective overshooting brings large amounts of moisture from the lower layer to the upper layer.

294 We conduct the Probability Density Function (PDF) analysis on the Near Surface Rain Rate (NSRR)

295 within convective overshooting, and that of total and convective precipitation are also calculated, shown

296 as Fig. 8. Grade of precipitation are as follows: Light rain: <4.9 mm/12 h, Moderate rain: 5.0-14.9

297 mm/12h, Heavy rain: 15.0-29.9 mm/12h, Torrential rain: 30.0-69.9 mm/12h, Downpour: 70.0-139.9

298 mm/12h, and Heavy downpour: ≥140.0 mm/12h (General Administration of Quality Supervision, 2012).

299 The PDF curve of NSRR of convective overshooting is clearly different from normal precipitation, and

300 has regional differences. The peak value of PDF of convective overshooting appears at ~10 mm/h,

301 classified as downpour, while that of normal precipitation appears at ~1 mm/h, classified as moderate

302 rain, which is obviously lower than convective overshooting. And the PDF of peak value of convective

303 overshooting over NC is about 11.5%, while that over MEC and SC are about 6%. Besides, sample size

304 of convective overshooting with precipitation grade of heavy downpour account for 34.0% (NC),46.7%

305 (MEC) and 34.8% (SC) respectively, 3-10 times than normal precipitation, which remind us to pay

306 special attention to the extreme precipitation events caused by convective overshooting that may cause

307 harm to our production and life.

308 **3.2.3 Microphysical features**

309 GPM center provides particle spectrum from dual-frequency radar. Based on the DSD profiles from

310 2ADPR, we further investigate the microphysical structures of convective overshooting. The Liquid

311 Water Path (LWP) and Ice Water Path (IWP) show the overall water content in the atmospheric column,

312   which is closely associated with microphysical processes within convective overshooting. To quantify

313   the characteristics of LWP and IWP within convective overshooting, the PDF of LWP and IWP of

314   convective overshooting are shown as Fig. 9, and that of convective and total precipitation are also

315   shown for comparison. The LWP and IWP within convective overshooting are the highest, with high

316   value of PDF mainly distributed around 1000 g/m^3 and 5000 g/m^3 respectively, much higher than that of

317   normal precipitation, which are around 100 g/m^3 and 300 g/m^3, indicating sufficient water vapor inside

318   convective overshooting. And differences of IWP between convective overshooting and normal

319   precipitation are bigger than LWP, suggesting that differences of water vapor above freezing level

320   between them is greater and convective overshooting brings water vapor from bottom of the troposphere

321   to higher layers. Besides, differences of LWP and IWP between three regions are also worth noting: The

322   LWP and IWP over MEC and SC are more similar and higher than NC. Especially, LWP over MEC has

323   a bimodal structure with peaks of 630 and 5000 g/m^3, which are consistent with the bimodal structure of

324   NSRR PDF curve in Fig. 8. Analysis above in Fig. 1b shows that tropopause height over northern MEC

325   is lower than southern MEC, making it easier for convective overshooting to occur over northern MEC.

326   This indicates that there are two types of convective overshooting events over MEC, weak events with

327   lower storm top height and strong events with higher storm top height, which correspond to the two

328   peaks of LWP PDF curve respectively.

329   We further use DSD parameter profiles, including the effective radius (D_0) and droplet concentration

330   (dBN_0) profiles, to analyze the microphysical characteristics within convective overshooting, shown as

331   Fig. 10. Results show that the microphysical processes within convective overshooting are unique,

332   leading to various properties of the droplets in precipitation. Droplets of convective overshooting are

333   large, but sparse. Influenced by strong updrafts, precipitation particles within convective overshooting

334   continuously collide and grow large enough to fall, therefore, the effective radius of droplets are big,

335   below 10 km altitude, almost exceeding 2.5 mm, which is about twice than that of normal precipitation.

336   However, the droplet concentration within convective overshooting is relatively lower. Differences of

337   microphysical structure between three regions are also worth noting. Convective overshooting events

338   over NC have large, but sparse droplets, while that over SC have small, but dense droplets, and the

339   effective radius and concentration of droplets over MEC are between NC and SC, which is speculated

340   that it's related to the differences of aerosol content and types over three regions. Specifically, at 1 km

341   altitude, the effective radius of droplets over NC is the largest (2.87 mm), followed by MEC (2.7 mm),

342   and SC is the lowest (2.5 mm). As altitude increases, the effective radius of droplets first increase and

343   then decrease, with maximum of 2.93 mm over NC at 2.5 km and sharp peak over MEC (2.85 mm) and

344   SC (2.76 mm) near freezing level, about twice than normal precipitation. The effective radius of droplets

345   for convective overshooting over NC and MEC are lower than 2.5 mm above 10 km and 12 km

346   respectively. It's worth noting that the effective radius of droplets for convective overshooting over SC

347   show an increasing trend above 8 km altitude, which are similar to convective precipitation, and their

348   effective radius of droplets over three regions also show an increasing tend from 9 km to 13 km, which

349   may be related to the strong upward motion inside. When the upward motion is strong, ice particles must

350   grow large enough to fall (Langmuir, 1948). Droplet concentration basically decreases with altitude, and

351   that within convective overshooting is obviously lower than normal precipitation and NC is the lowest,

352   while MEC and SC are higher and similar. Droplet concentration within convective overshooting near

353   ground is the highest, with NC (25.4), MEC (28) and SC (28), while that of normal precipitation is

354   mainly distributed between 32 and 35.

355   **4 Summary and conclusions**

356   The microphysical characteristics of convective overshooting are essential but poorly understood due to

357   the difficulty in accurately detecting the convective overshooting and obtaining microphysical

358   parameters during severe weather events. Based on the microphysical precipitation data from GPM DPR

359   and the meteorological data from ERA5 data, we designed a more accurate algorithm for convective

360   overshooting determination and examine the particle size, concentration, phase state and other

361   parameters of the convective overshooting over East China. The main conclusions are:

362   Firstly, the horizontal distribution characteristics of convective overshooting over East China are

363   analysed by designing a more accurate algorithm for convective overshooting determination. Statistical

364   results indicate that the frequency of the convective overshooting over East China is very low, with a

365   magnitude of only 10^{-3}, with large regional differences. Convective overshooting events occur more

366   frequently over NC and northern MEC, than SC and southern MEC, mainly because of the lower

367   tropopause height of the former and the different underlying surfaces. The mean convective overshooting

368   storm top height mostly ranges from 10 km to 21 km and has obvious regional distribution differences,

369   and convective overshooting storm top height over NC is 5-6 km higher than SC.

370 Based on the reflectivity profiles and the rain-rate profiles provided by the GPM DPR instrument, we

371 studied the vertical structure of precipitation within convective overshooting. The CFADs analysis of the

372 radar reflectivity shows that radar reflectivity within convective overshooting is stronger and its storm

373 top height is higher. The CFADs analysis also shows regional differences. Radar reflectivity of

374 convective overshooting over NC accounts for a higher proportion below the freezing level, while MEC

375 and SC account for a higher proportion above the freezing level, which indicate that the upward motion

376 within convective overshooting over MEC and SC are stronger and there are more ice crystal particles.

377 Rain rate results also show that rain rate within convective overshooting is higher, 5-10 times than that of

378 normal precipitation. Especially, sample number of strong precipitation with grade of precipitation of

379 heavy downpour accounts for 34.0% (NC), 46.7% (MEC), and 34.8% (SC), which remind us to pay

380 special attention to the extreme precipitation events caused by convective overshooting.

381 GPM center provides particle spectrum from dual-frequency radar. Based on the DSD profiles from

382 2ADPR, we further investigated the microphysical structures of convective overshooting. Statistical

383 results show that convective overshooting has unique microphysical characteristics compared with

384 normal precipitation, with obvious regional differences. The LWP and IWP within convective

385 overshooting are abundant, with high values of PDF distributed around 1000 g/m^3 and 5000 g/m^3

386 respectively. Moreover, influenced by strong updrafts, precipitation particles within convective

387 overshooting continuously collide and grow large enough to fall, therefore, the effective radius is big,

388 below 10 km altitude, almost exceeding 2.5 mm, which is about twice than that of normal precipitation.

389 However, the droplet concentration within convective overshooting is relatively lower. Differences of

390 microphysical structure between three regions are also worth noting. The effective radius of droplet over

391 NC is slightly bigger than MEC and SC, while the droplet concentration is lower, which is speculated

392 that it's related to the differences of aerosol content and types over three regions.

393 Quantitative study of the internal microphysical characteristics within convective overshooting has not

394 been documented previously. Findings of this study may have important implications for the

395 microphysical evolution associated with convective overshooting, and provide more accurate

396 precipitation microphysical parameters as the input of the model simulation. This study is the

397 continuation of the previous research (Sun et al., 2021). In the future, we will further explore the impact

398 of aerosol on the internal microphysical characteristics within convective overshooting, and more

399 microphysical parameters with higher spatiotemporal resolution are expected to provide more detailed

400 features.

401 **Data availability.** ERA5 data are taken from
402 https://www.ecmwf.int/en/forecasts/datasets/reanalysis-datasets/era5. GPM DPR data are archived at
403 https://gpm.nasa.gov/data/directory.

404 **Acknowledgements.** This work was funded by the National Natural Science Foundation of China
405 Project (Grant No. 42230612) and the fellowship of China Postdoctoral Science Foundation (Grant
406 Numbers: 2022M723011).

407 **Author contributions.** Sun N., Lu G.P., and Fu Y.F. framed up this study. All the authors discussed the
408 concepts. Sun N. conducted the data analyses. Sun N. drafted the manuscript and all authors edited the
409 manuscript.

410 **Competing interests.** The authors declare no competing interests.

411 **References**

412 Anderson, J. G., Wilmouth, D. M., Smith, J. B. and Sayres, D. S.: UV dosage levels in summer:
413   Increased risk of ozone loss from convectively injected water vapor, Science, 337, 835-839,
414   https://doi.org/10.1126/science.1222978, 2012.

415 Avery, M. A., Davis, S. M., Rosenlof, K. H., Ye, H. and Dessler, A. E.: Large anomalies in lower
416   stratospheric water vapour and ice during the 2015–2016 El Niño, Nature Geoscience, 10, 405-409,
417   https://doi.org/10.1038/ngeo2961, 2017.

418 Alcala, C. M. and Dessler, A. E.: Observations of deep convection in the tropics using the Tropical
419   Rainfall Measuring Mission (TRMM) precipitation radar, Journal of Geophysical Research:
420   Atmospheres, 107, 4792, https://doi.org/10.1029/2002JD002457, 2002.

421 Biondi, R., Randel, W. J., Ho, S. P., Neubert, T. and Syndergaard, S.: Thermal structure of intense
422   convective clouds derived from GPS radio occultations, Atmospheric Chemistry and Physics, 12,
423   5309-5318, https://doi.org/10.5194/acp-12-5309-2012, 2012.

424 Bedka, K., Murillo, E. M., Homeyer, C. R., Scarino, B. and Mersiovsky, H.: The above-anvil cirrus
425   plume: An important severe weather indicator in visible and infrared satellite imagery, Weather and
426   Forecasting, 33, 1159-1181, https://doi.org/10.1175/WAF-D-18-0040.1, 2018.

427   Bethan, S., Vaughan, G., and Reid, S. J.: A comparison of ozone and thermal tropopause heights and the

428   impact of tropopause definition on quantifying the ozone content of the troposphere, Quarterly

429   Journal of the Royal Meteorological Society, 122(532), 929-944,

430   https://doi.org/10.1002/qj.49712253207, 1996.

431   Brunner, J. C., Ackerman, S. A., Bachmeier, A. S. and Rabin, R. M.: A quantitative analysis of the

432   enhanced-V feature in relation to severe weather, Weather and Forecasting, 22, 853-872,

433   https://doi.org/10.1175/WAF1022.1, 2007.

434   Bedka, K. M.: Overshooting cloud top detections using MSG SEVIRI Infrared brightness temperatures

435   and their relationship to severe weather over Europe, Atmospheric Research, 99, 175-189,

436   https://doi.org/10.1016/j.atmosres.2010.10.001, 2011.

437   Chaboureau, J. P., Cammas, J. P., Duron, J., Mascart, P. J., Sitnikov, N. M. and Voessing, H. J.: A

438   numerical study of tropical cross-tropopause transport by convective overshoots, Atmospheric

439   Chemistry and Physics, 7, 1731-1740, https://doi.org/10.5194/acp-7-1731-2007, 2007.

440   Corti, T., Luo, B. P. and De Reus, M. et al.: Unprecedented evidence for deep convection hydrating the

441   tropical stratosphere, Geophysical Research Letters, 35, L10810,

442   https://doi.org/10.1029/2008GL033641, 2008.

443   Chemel, C., Russo, M. R., Pyle, J. A., Sokhi, R. S. and Schiller, C.: Quantifying the imprint of a severe

444   hector thunderstorm during ACTIVE/SCOUT-O3 onto the water content in the upper

445   troposphere/lower stratosphere, Monthly weather review, 137, 2493-2514,

446   https://doi.org/10.1175/2008MWR2666.1, 2009.

447   Chae, J. H., Wu, D. L., Read, W. G. and Sherwood, S. C.: The role of tropical deep convective clouds on

448   temperature, water vapor, and dehydration in the tropical tropopause layer (TTL), Atmospheric

449   Chemistry and Physics, 11, 3811-3821, https://doi.org/10.5194/acp-11-3811-2011, 2011.

450   Danielsen, E. F.: In situ evidence of rapid, vertical, irreversible transport of lower tropospheric air into

451   the lower tropical stratosphere by convective cloud turrets and by larger‐scale upwelling in tropical

452   cyclones, Journal of Geophysical Research: Atmospheres, 98, 8665-8681,

453   https://doi.org/10.1029/92JD02954, 1993.

454   De Reus, M., Borrmann, S. and Bansemer, A. et al: Evidence for ice particles in the tropical stratosphere

455   from in-situ measurements, Atmospheric Chemistry and Physics, 9, 6775-6792,

456   https://doi.org/10.5194/acp-9-6775-2009, 2009.

457   Danielsen, E. F., Hipskind, R. S. and Gaines, S. E. et al.: Three-dimensional analysis of potential

458   vorticity associated with tropopause folds and observed variations of ozone and carbon monoxide,

459   Journal of Geophysical Research: Atmospheres, 92(D2), 2103-2111,

460   https://doi.org/10.1029/JD092iD02p02103, 1987.

461   Dworak, R., Bedka, K., Brunner, J. and Feltz, W.: Comparison between GOES-12 overshooting-top

462   detections, WSR-88D radar reflectivity, and severe storm reports, Weather and Forecasting, 27,

463   684-699, https://doi.org/10.1175/WAF-D-11-00070.1, 2012.

464   Fueglistaler, S., Wernli, H. and Peter, T.: Tropical troposphere‐to‐stratosphere transport inferred from

465   trajectory calculations, Journal of Geophysical Research: Atmospheres, 109, D03108,

466   https://doi.org/10.1029/2003JD004069, 2004.

467   Fujita, T. T.: The Teton-Yellowstone tornado of 21 July 1987, Monthly Weather Review, 117,

468   1913-1940, https://doi.org/10.1175/1520-0493(1989)117<1913:TTYTOJ>2.0.CO;2, 1989.

469   Frey, W., Schofield, R. and Hoor, P. et al.: The impact of overshooting deep convection on local

470   transport and mixing in the tropical upper troposphere/lower stratosphere (UTLS), Atmospheric

471   Chemistry and Physics, 15, 6467-6486, https://doi.org/10.5194/acp-15-6467-2015, 2015.

472   General Administration of Quality Supervision, Inspection and Quarantine of the People's Republic of

473   China: Standardization Administration of the People's Republic of China, GB/T 28592—2012 Grade

474   of precipitation, Standards Press of China, 2012.

475   Grosvenor, D. P., Choularton, T. W., Coe, H. and Held, G.: A study of the effect of overshooting deep

476   convection on the water content of the TTL and lower stratosphere from Cloud Resolving Model

477   simulations, Atmospheric Chemistry and Physics, 7, 4977-5002,

478   https://doi.org/10.5194/acp-7-4977-2007, 2007.

479   Gettelman, A., Salby, M. L. and Sassi, F.: Distribution and influence of convection in the tropical

480   tropopause region, Journal of Geophysical Research: Atmospheres, 107, 4080,

481   https://doi.org/10.1029/2001JD001048, 2002.

482   Homeyer, C. R. and Kumjian, M. R.: Microphysical characteristics of overshooting convection from

483   polarimetric radar observations, Journal of the Atmospheric Sciences, 72, 870-891,

484   https://doi.org/10.1175/JAS-D-13-0388.1, 2015.

485   Hoffmann, L., Günther, G. and Li, D. et al.: From ERA-Interim to ERA5: the considerable impact of

486   ECMWF's next-generation reanalysis on Lagrangian transport simulations, Atmospheric Chemistry

487   and Physics, 19, 3097-3124, https://doi.org/10.5194/acp-19-3097-2019, 2019.

488   Highwood, E. J. and Hoskins, B. J.: The tropical tropopause, Quarterly Journal of the Royal

489   Meteorological Society, 124, 1579-1604, https://doi.org/10.1002/qj.49712454911, 1998.

490   Holton, J. R., Haynes, P. H. and McIntyre, M. E. et al.: Stratosphere-troposphere exchange. Reviews of

491   geophysics, 33(4), 403-439, https://doi.org/10.1029/95RG02097, 1995.

492   Jensen, E. J., Ackerman, A. S. and Smith, J. A.: Can overshooting convection dehydrate the tropical

493   tropopause layer?, Journal of Geophysical Research: Atmospheres, 112, D11209,

494   https://doi.org/10.1029/2006JD007943, 2007.

495   Johnston, B. R., Xie, F. and Liu, C.: The effects of deep convection on regional temperature structure in

496   the tropical upper troposphere and lower stratosphere, Journal of Geophysical Research:

497   Atmospheres, 123, 1585-1603, https://doi.org/10.1002/2017JD027120, 2018.

498   Khaykin, S., Pommereau, J. P. and Korshunov, L. et al.: Hydration of the lower stratosphere by ice

499   crystal geysers over land convective systems, Atmospheric Chemistry and Physics, 9, 2275-2287,

500   https://doi.org/10.5194/acp-9-2275-2009, 2009.

501   Kellenbenz, D. J., Grafenauer, T. J. and Davies, J. M.: The North Dakota tornadic supercells of 18 July

502   2004: Issues concerning high LCL heights and evapotranspiration, Weather and forecasting, 22,

503   1200-1213, https://doi.org/10.1175/2007WAF2006109.1, 2007.

504   Langmuir, I.: The production of rain by a chain reaction in cumulus clouds at temperatures above

505   freezing, Journal of the Atmospheric Sciences, 5(5), 175-192,

506   https://doi.org/10.1175/1520-0469(1948)005<0175:TPORBA>2.0.CO;2, 1948.

507   Lane, T. P. and Sharman, R. D.: Gravity wave breaking, secondary wave generation, and mixing above

508   deep convection in a three‐dimensional cloud model, Geophysical Research Letters, 33.

509   https://doi.org/10.1029/2006GL027988, 2006.

510   Lane, T. P., Sharman, R. D., Clark, T. L. and Hsu, H. M.: An investigation of turbulence generation

511   mechanisms above deep convection, Journal of the atmospheric sciences, 60, 1297-1321,

512   https://doi.org/10.1175/1520-0469(2003)60<1297:AIOTGM>2.0.CO;2, 2003.

513 Liu, N. and Liu, C.: Global distribution of deep convection reaching tropopause in 1 year GPM

514 observations, Journal of Geophysical Research: Atmospheres, 121, 3824-3842,

515 https://doi.org/10.1002/2015JD024430, 2016.

516 Liu, N., Liu, C. and Hayden, L.: Climatology and detection of overshooting convection from 4 years of

517 GPM precipitation radar and passive microwave observations, Journal of Geophysical Research:

518 Atmospheres, 125, e2019JD032003, https://doi.org/10.1029/2019JD032003, 2020.

519 Liu, C. and Zipser, E. J.: Global distribution of convection penetrating the tropical tropopause, Journal of

520 Geophysical Research: Atmospheres, 110, D23104, https://doi.org/10.1029/2005JD006063, 2005.

521 Liu, P., Wang, Y., Feng, S., Li, C. Y. and Fu, Y. F.: Climatological characteristics of overshooting

522 convective precipitation in summer and winter over the tropical and subtropical regions, Chin. J.

523 Atmos. Sci., 36, 579-589, https://doi.org/10.3878/j.issn.1006-9895.2011.11109, 2012.

524 Line, W. E., Schmit, T. J., Lindsey, D. T. and Goodman, S. J.: Use of geostationary super rapid scan

525 satellite imagery by the Storm Prediction Center, Weather and Forecasting, 31, 483-494,

526 https://doi.org/10.1175/WAF-D-15-0135.1, 2016.

527 Machado, L. A. T., Rossow, W. B., Guedes, R. L. and Walker, A. W.: Life cycle variations of mesoscale

528 convective systems over the Americas, Monthly Weather Review, 126, 1630-1654,

529 https://doi.org/10.1175/1520-0493(1998)126<1630:LCVOMC>2.0.CO;2, 1998.

530 Muhsin, M., Sunilkumar, S. V., Ratnam, M. V., Parameswaran, K., Murthy, B. K. and Emmanuel, M.:

531 Effect of convection on the thermal structure of the troposphere and lower stratosphere including the

532 tropical tropopause layer in the South Asian monsoon region, Journal of Atmospheric and

533 Solar-Terrestrial Physics, 169, 52-65, https://doi.org/10.1016/j.jastp.2018.01.016, 2018.

534 Marion, G. R., Trapp, R. J. and Nesbitt, S. W.: Using overshooting top area to discriminate potential for

535 large, intense tornadoes, Geophysical Research Letters, 46, 12520-12526,

536 https://doi.org/10.1029/2019GL084099, 2019.

537 McCann, D. W.: The enhanced-V: A satellite observable severe storm signature, Monthly Weather

538 Review, 111, 887-894, https://doi.org/10.1175/1520-0493(1983)111<0887:TEVASO>2.0.CO;2,

539 1983.

540 Negri, A. J. and Adler, R. F.: Relation of satellite-based thunderstorm intensity to radar-estimated

541 rainfall, Journal of Applied Meteorology and Climatology, 20, 288-300,

542 https://doi.org/10.1175/1520-0450(1981)020<0288:ROSBTI>2.0.CO;2, 1981.

543   Reynolds, D. W.: Observations of damaging hailstorms from geosynchronous satellite digital

544   data, Monthly Weather Review, 108, 337-348,

545   https://doi.org/10.1175/1520-0493(1980)108<0337:OODHFG>2.0.CO;2, 1980.

546   Rodriguez‑Franco, J. J. and Cuevas, E.: Characteristics of the subtropical tropopause region based on

547   long‑term highly resolved sonde records over Tenerife, Journal of Geophysical Research:

548   Atmospheres, 118, 10-754, https://doi.org/10.1002/jgrd.50839, 2013.

549   Rossow, W. B. and Pearl, C.: 22‑year survey of tropical convection penetrating into the lower

550   stratosphere, Geophysical research letters, 34, L04803, https://doi.org/10.1029/2006GL028635,

551   2007.

552   Setvák, M., Lindsey, D. T. and Novák, P. et al.: Satellite-observed cold-ring-shaped features atop deep

553   convective clouds, Atmospheric Research, 97, 80-96, https://doi.org/10.1016/j.atmosres.2010.03.009,

554   2010.

555   Solomon, S., Rosenlof, K. H. and Portmann, R. W. et al.: Contributions of stratospheric water vapor to

556   decadal changes in the rate of global warming, Science, 327, 1219-1223,

557   https://doi.org/10.1126/science.1182488, 2010.

558   Sherwood, S. C. and Dessler, A. E.: A model for transport across the tropical tropopause, Journal of the

559   Atmospheric Sciences, 58, 765-779,

560   https://doi.org/10.1175/1520-0469(2001)058<0765:AMFTAT>2.0.CO;2, 2001.

561   Smith, J. B., Wilmouth, D. M., and Bedka, K. M. et al.: A case study of convectively sourced water

562   vapor observed in the overworld stratosphere over the United States, Journal of Geophysical

563   Research: Atmospheres, 122(17), 9529-9554, https://doi.org/10.1002/2017JD026831, 2017.

564   Sun, N., Fu, Y., Zhong, L., Zhao, C. and Li, R.: The Impact of Convective Overshooting on the Thermal

565   Structure over the Tibetan Plateau in Summer Based on TRMM, COSMIC, Radiosonde, and

566   Reanalysis Data, Journal of Climate, 34, 8047-8063, https://doi.org/10.1175/JCLI-D-20-0849.1,

567   2021.

568   Sun, N., Fu, Y., Zhong, L. and Li, R.: Aerosol effects on the vertical structure of precipitation in East

569   China, npj Climate and Atmospheric Science, 5, 60, https://doi.org/10.1038/s41612-022-00284-0,

570   2022a.

Sun, N., Zhong, L., Zhao, C., Ma, M. and Fu, Y.: Temperature, water vapor and tropopause characteristics over the Tibetan Plateau in summer based on the COSMIC, ERA-5 and IGRA datasets, Atmospheric Research, 266, 105955, https://doi.org/10.1016/j.atmosres.2021.105955, 2022b.

Sherwood, S. C., Horinouchi, T. and Zeleznik, H. A.: Convective impact on temperatures observed near the tropical tropopause, Journal of Atmospheric Sciences, 60, 1847-1856, https://doi.org/10.1175/1520-0469(2003)060<1847:CIOTON>2.0.CO;2, 2003.

Takahashi, H. and Luo, Z. J.: Characterizing tropical overshooting deep convection from joint analysis of CloudSat and geostationary satellite observations, Journal of Geophysical Research: Atmospheres, 119, 112-121, https://doi.org/10.1002/2013JD020972, 2014.

Wang, X., Huang, Y., and Qu, Z. et al.: Convectively Transported Water Vapor Plumes in the Midlatitude Lower Stratosphere, Journal of Geophysical Research: Atmospheres, 128(4), e2022JD037699, https://doi.org/10.1029/2022JD037699, 2023.

Werner, F., Schwartz, M. J., and Livesey, N. J. et al.: Extreme outliers in lower stratospheric water vapor over North America observed by MLS: Relation to overshooting convection diagnosed from colocated Aqua‐MODIS data, Geophysical Research Letters, 47(24), e2020GL090131, https://doi.org/10.1029/2020GL090131, 2020.

World Meteorological Organization.: Meteorology—A three‐dimensional science: Second session of the commission for aerology, WMO Bull, 4, 134-138, 1957.

Xia, J.: Research on climatic regionalization of China and characteristics of temperature, humidity and wind in precipitation cloud, University of Science and Technology of China, 2015.

Xu, W.: Thunderstorm climatologies and their relationships to total and extreme precipitation in China, Journal of Geophysical Research: Atmospheres: 125, e2020JD033152, https://doi.org/10.1029/2020JD033152, 2020.

Yuter, S. E. and Houze, R. A.: Three-dimensional kinematic and microphysical evolution of Florida cumulonimbus. Part II: Frequency distributions of vertical velocity, reflectivity, and differential reflectivity, Monthly Weather Review, 123(7), 1941-1963, https://doi.org/10.1175/1520-0493(1995)123<1941:TDKAME>2.0.CO;2, 1995.

Zhang, A. and Fu, Y.: Life cycle effects on the vertical structure of precipitation in East China measured by Himawari-8 and GPM DPR, Monthly Weather Review, 146, 2183-2199, https://doi.org/10.1175/MWR-D-18-0085.1, 2018.

601 Zahn, A., Brenninkmeijer, C. A. M., and Van Velthoven, P. F. J.: Passenger aircraft project CARIBIC

602   1997–2002, Part I: the extratropical chemical tropopause, Atmospheric Chemistry and Physics

603   Discussions, 4(1), 1091-1117, https://doi.org/10.5194/acpd-4-1091-2004, 2004.

604

Tables

Table1. The sample number of total precipitation, convective precipitation, and convective overshooting over NC, MEC, and SC.

Sample number (count, ct)	NC	MEC	SC
Total Precipitation	652489	546313	319127
Convective Precipitation	111903	137674	111900
Convective Overshooting	2394	582	296

614   **Figures**

615
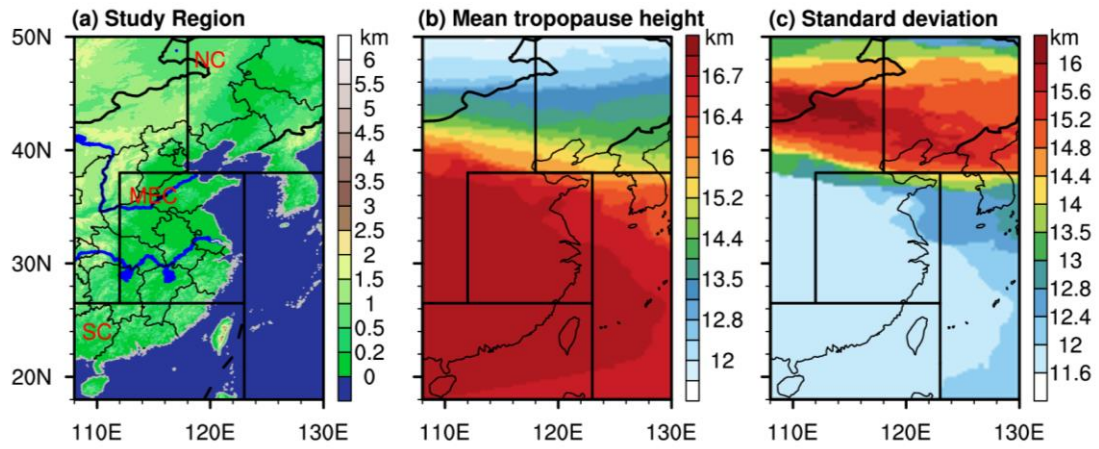
616
617   **Figure 1.** Study areas and their tropopause characteristics. **(a)** Regionalization of East China (Black boxes:
618   Divisions between NC, MEC and SC, and only the land surface is studied) and their terrain features. **(b)**
619   Climatological mean of tropopause height from 2014 to 2020 in summer (June, July and August). **(c)** Distribution
620   of standard deviation of tropopause height.

621

622
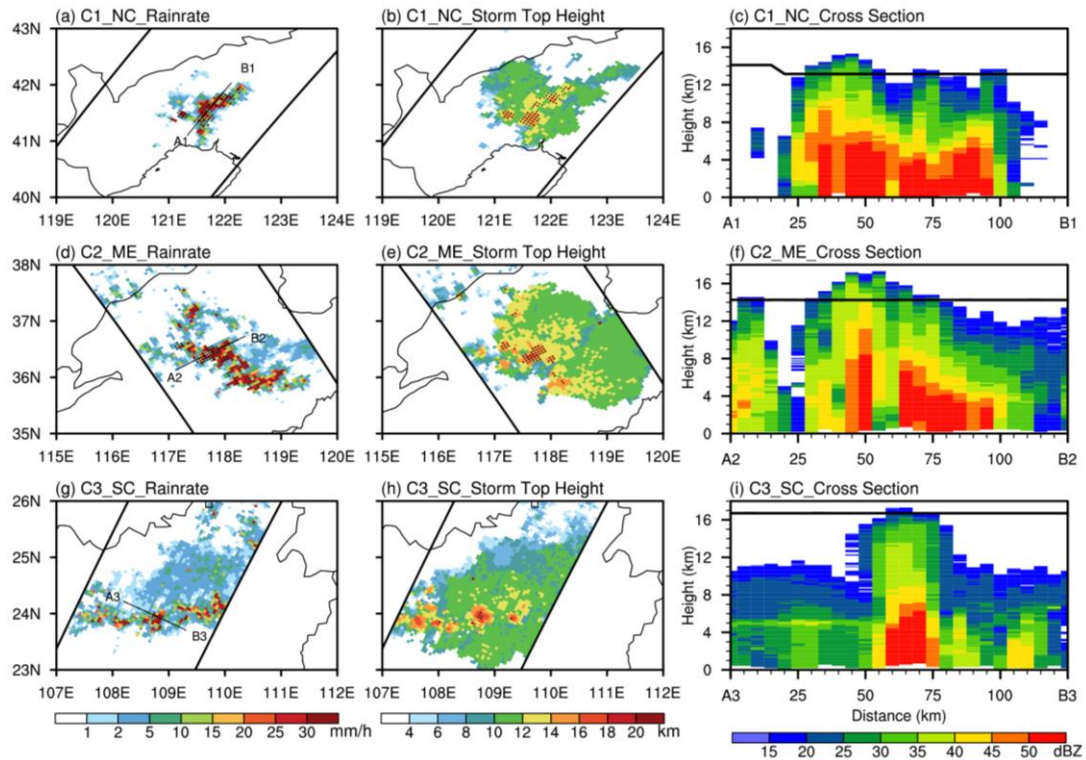
Figure 2. Precipitation characteristics of convective overshooting cases. **(a)** Distribution of rain rate of Case 1 (C1).
(The pixels in which convective overshooting occurs are marked as black points). **(b)** Distribution of storm top
height of C1. **(c)** Radar reflectivity cross section along A1B1 and the black line show the tropopause height along
A1B1. **(d)** Distribution of rain rate of C2. **(e)** Distribution of storm top height of C2. **(f)** Radar reflectivity cross
section along A2B2. **(g)** Distribution of rain rate of C3. **(h)** Distribution of storm top height of C3. **(i)** Radar
reflectivity cross section along A3B3.

629
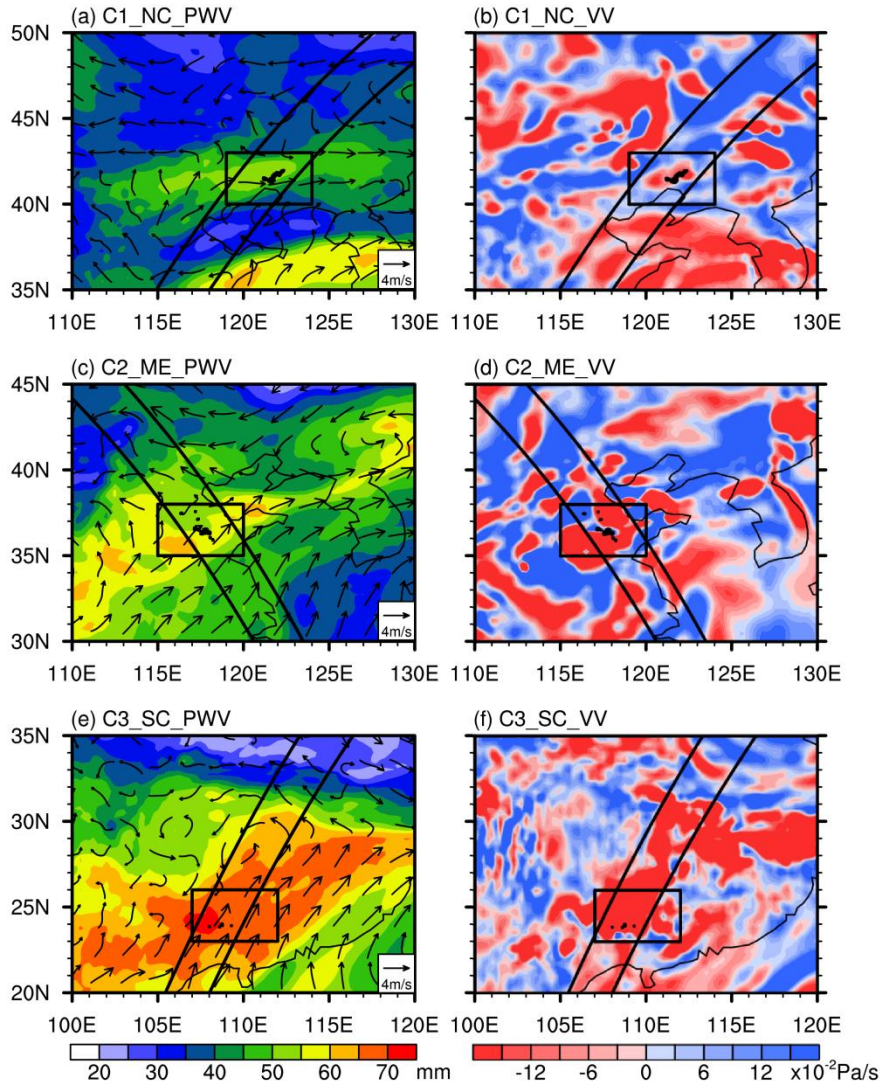
Figure 3. Characteristics of large scale circulation of convective overshooting cases. **(a)** Distribution of precipitable water vapor (PWV) and streamlines at 850 hPa of C1. The area where the case occurred is marked as big black boxes and the pixels in which convective overshooting occurs are marked as little black boxes. The black line is the GPM detection orbit. **(b)** Distribution of vertical velocity (VV) at 500 hPa of C1. **(c)** Distribution of PWV and streamlines of C2. **(d)** Distribution of VV of C2. **(e)** Distribution of PWV and streamlines of C3. **(f)** Distribution of VV of C3.
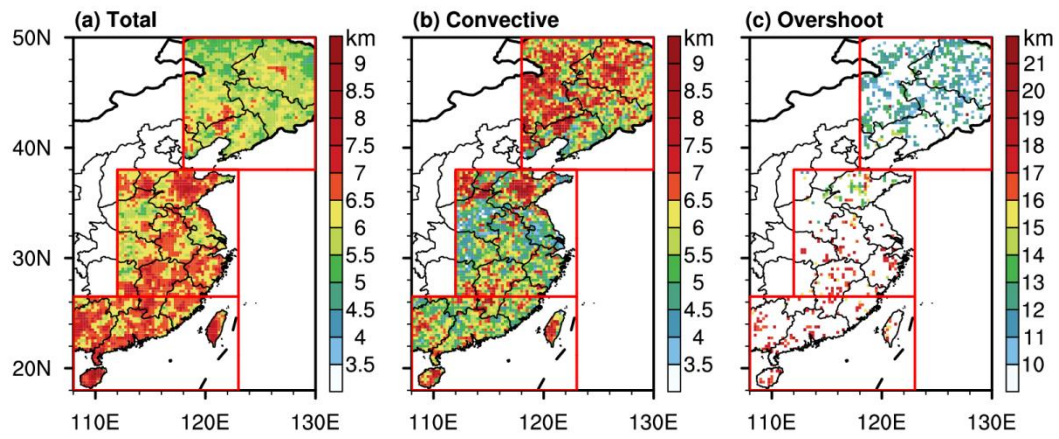
638

639 **Figure 4.** Geographical distribution of storm top height. **(a)** Distribution of storm top height for total precipitation.

640 **(b)** Distribution of storm top height for convective precipitation. **(c)** Distribution of storm top height for convective

641 overshooting.

642
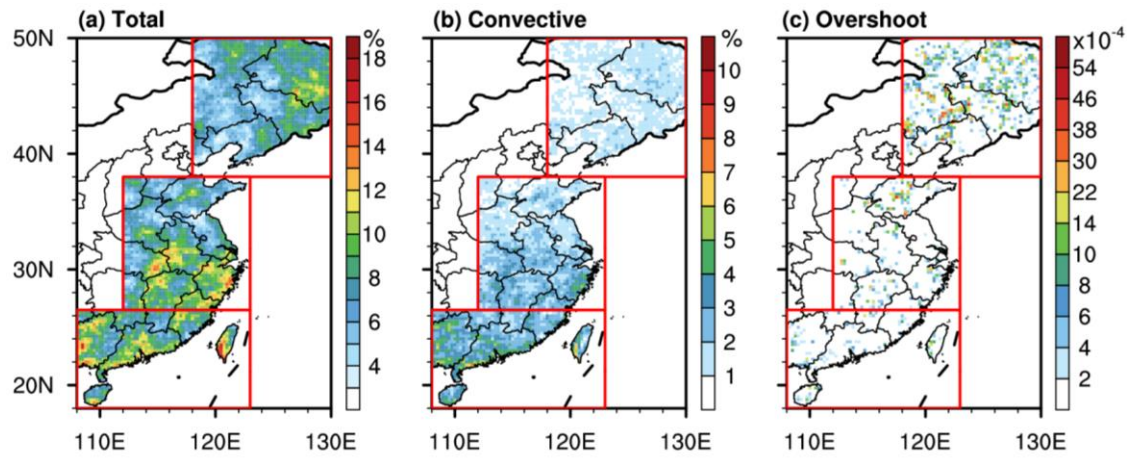
Figure 5. Precipitation frequency. **(a)** Frequency of total precipitation. **(b)** Frequency of convective precipitation. **(c)** Frequency of convective overshooting.
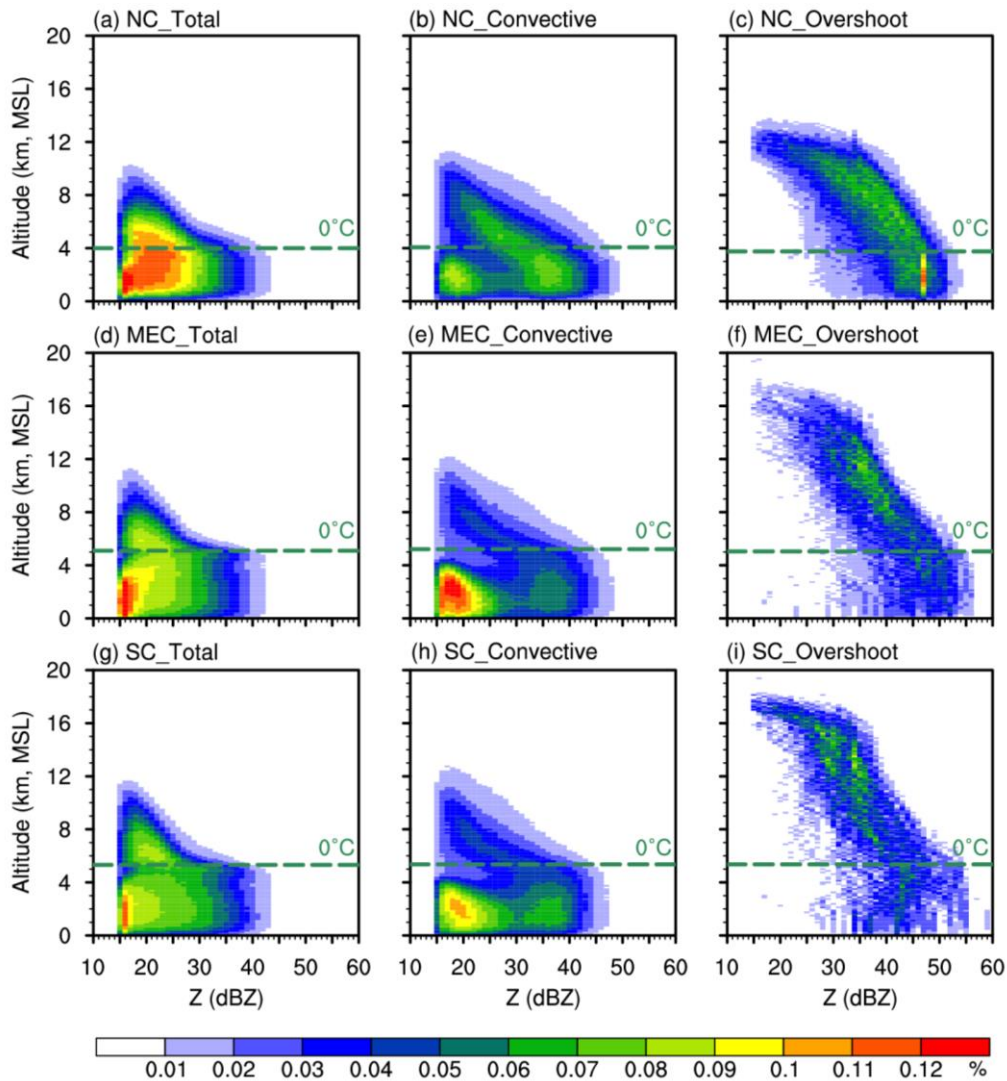
Figure 6. Contoured Frequency by Altitude Diagrams (CFADs) of radar reflectivity. **(a)** CFADs for total precipitation over NC (Green dotted line indicates the altitude of the freezing level). **(b)** CFADs for convective precipitation over NC. **(c)** CFADs for convective overshooting over NC. **(d)** CFADs for total precipitation over MEC. **(e)** CFADs for convective precipitation over MEC. **(f)** CFADs for convective overshooting over MEC. **(g)** CFADs for total precipitation over SC. **(h)** CFADs for convective precipitation over SC. **(i)** CFADs for convective overshooting over SC.

655
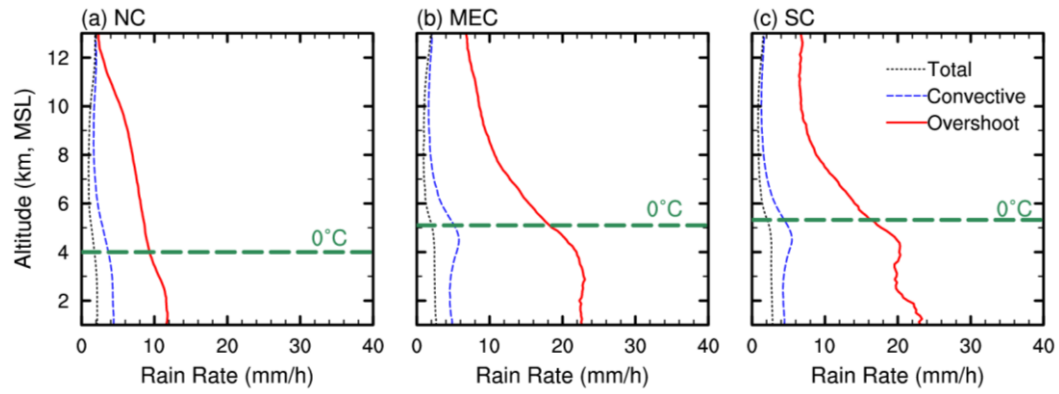
656 **Figure 7.** Rain rate profiles for total precipitation, convective precipitation and convective overshooting (Red lines

657 are convective overshooting; Blue lines are the convective precipitation; Black lines are the total precipitation). **(a)**

658 The rain rate profiles over NC (Green dotted line indicates the altitude of the freezing level). **(b)** The rain rate

659 profiles over MEC. **(c)** The rain rate profiles over SC.

660
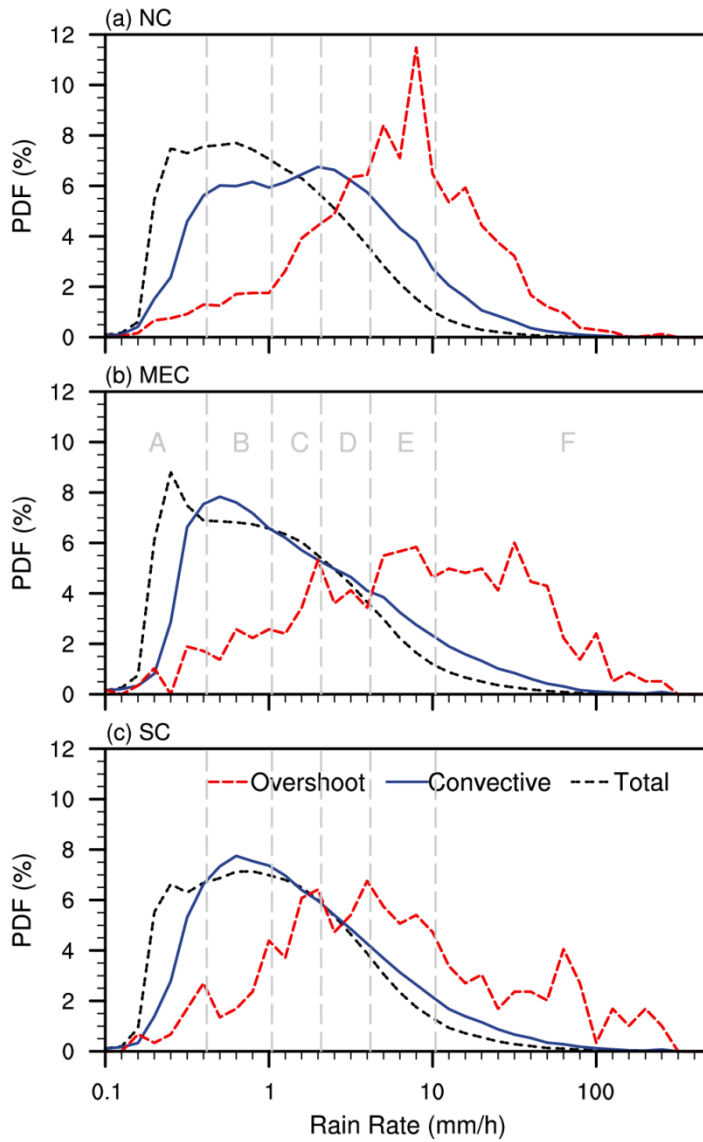
Figure 8. Probability Density Function (PDF) of Near Surface Rain Rate (NSRR). **(a)** PDF of NSRR in NC. **(b)** PDF of NSRR in MEC. **(c)** PDF of NSRR in SC.
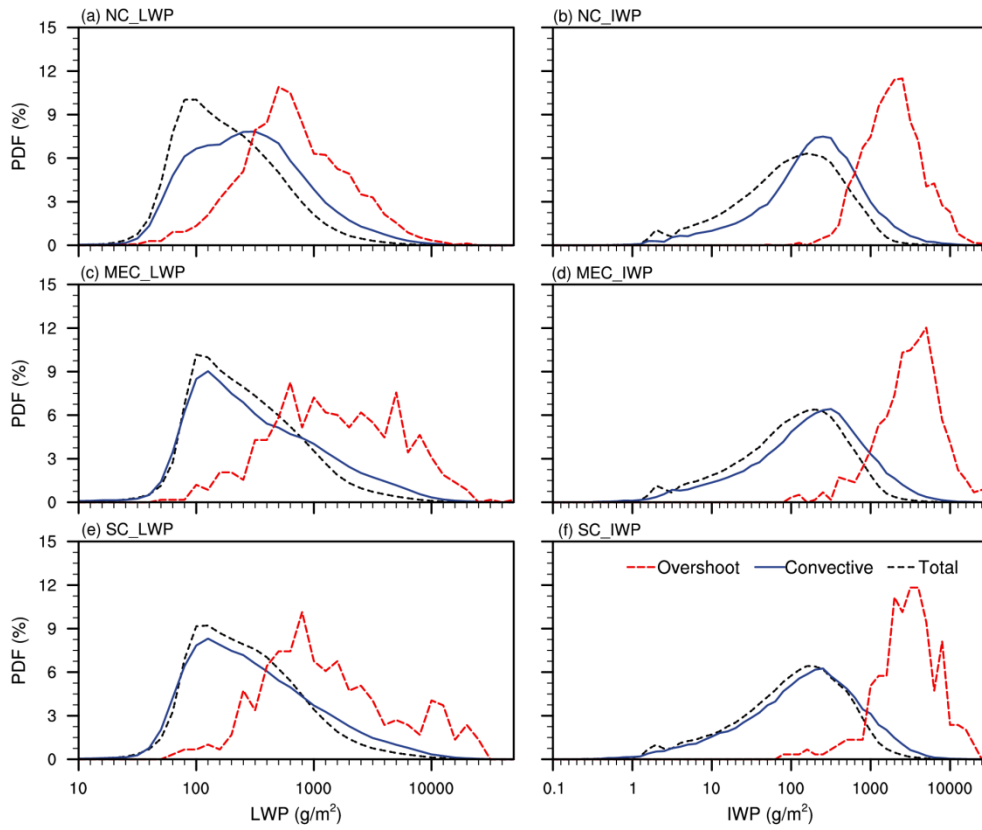
664
665 **Figure 9.** PDF of Liquid Water Path (LWP) and Ice Water Path (IWP). **(a)** PDF of LWP over NC. **(b)** PDF of IWP
666 over NC. **(c)** PDF of LWP over MEC. **(d)** PDF of IWP over MEC. **(e)** PDF of LWP over SC. **(f)** PDF of IWP over
667 SC.
668
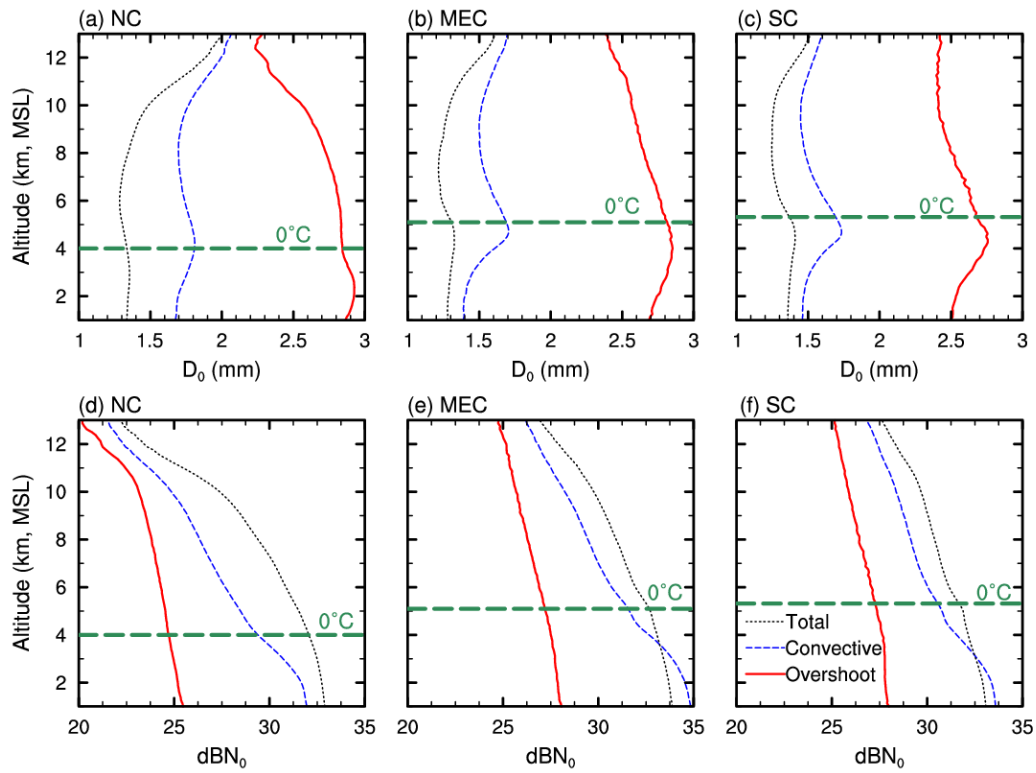
669

670 **Figure 10.** The droplet concentration (dBN$_0$) and effective radius (D$_0$) profiles for total precipitation, convective

671 precipitation and convective overshooting over NC, MEC and SC. **(a)** The dBN$_0$ profiles over NC (Green dotted

672 line indicates the altitude of the freezing level). **(b)** The dBN$_0$ profiles over MEC. **(c)** The dBN$_0$ profiles over SC.

673 **(d)** D$_0$ profiles over NC. **(e)** D$_0$ profiles over MEC. **(f)** D$_0$ profiles over SC.